Impact melting upon basin formation on early Mars.

Lukas Manske[1,2], Simone Marchi[3], Ana-Catalina Plesa[4], Kai Wünnemann[1,2]

[1]Museum für Naturkunde Berlin, Leibniz Institute for Evolution and Biodiversity Science, Invalidenstraße 43, 10115 Berlin, Germany

[2]Freie Universität Berlin, Institut für Geologische Wissenschaften, Malteserstraße 74 - 100, 12249 Berlin, Germany

[3]Southwest Research Institute, 1050 Walnut St., Boulder, Colorado 80302 USA

[4]German Aerospace Center (DLR), Rutherfordstraße 2, 12489 Berlin, Germany

Keywords:
Impact processes
Cratering
Mars
Collisional physics

Abstract: The early bombardment history of Mars may have drastically shaped its crustal evolution. Impact-induced melting of crustal and mantle materials leads to the formation of local and regional melt ponds, and the cumulative effects of the impact flux could result in widespread melting of the crust. To quantify impact-melt production, its provenance and final distribution as a function of impact conditions, we carried out a systematic parameter study using the iSALE shock physics code. In contrast to simplified scaling laws for estimating the amount of melt generated by shock compression, we take the planet's thermal state at the time of impact into account. In addition, we consider decompression melting as a consequence of lithostatic uplift of initially deep-seated material. We find that the geothermal profile has a strong effect on melt production, and that melt volumes are significantly increased by up to a factor of seven in comparison to existing analytical estimates. Enhanced melting occurs at impactor sizes (and velocities) that deposit most of their energy at a depth close to the base of the lithosphere. Impactors larger than 10 km penetrate through the lithosphere and can generate a significant amount of melt by decompression due to lithostatic uplift, which can make up to 40% of the total melt volume. In some cases, the total melt volume exceeds the volume of the transient (and final) crater and the surface expression of these collisions may resemble large igneous provinces rather than typical craters.

1. Introduction:

The cratered surface of Mars bears scars of collisions that have occurred throughout its history. Mars is considered to have accreted the bulk of its mass within about 5 million years after the condensation of the first solids (Dauphas and Pourmand 2011; Kleine and Walker 2017). This "primary accretion" phase was followed by a period of time in which collisions were less frequent and less energetic, named "late accretion". The total mass added to Mars during the late accretion is estimated to be about 0.25% of the planet's mass (Walker 2009), based on the abundance of highly siderophile elements in martian meteorites. The details of the late accretion are debated. Mars' number of large craters (>150 km in diameter) is lower than expected based on extrapolations from the Moon, at odds with a rapid formation of Mars. To explain the paucity of large craters, a recent work suggests that Mars experienced a lull in the impact flux post Borealis formation, considered to have formed prior to ~4.5 Ga (Bottke and Andrews-Hanna 2017). An alternative model (Morbidelli et al. 2018) envisions a late formation of Borealis basin (~4.3 Ga) which could have been responsible for the obliteration of many older large craters. In addition, a closer examination of large-scale impact mixing suggests that Mars could have accreted up to 2.5% of its mass. The latter may also partially explain the heterogeneous W isotopes in martian meteorites (Marchi et al. 2020).

To achieve a better understanding of the early bombardment history of Mars and its paucity of large craters, it is important to consider the extent of melting of crustal and mantle materials resulting from large impact events. Previous studies suggest that, in case of very large impacts, the generated melt volume can exceed the crater volume (e.g., Grieve et al. 2006) leading to localized igneous provinces rather than morphologies typical of impact structures or basins (Tonks and Melosh 1993). These results may affect our ability to identify ancient craters, with implications for the earliest cratering history.

The extent of impact-induced melt generated throughout the early history of Mars may be estimated by simplified scaling laws, which predict melt volumes as a function of impact parameters. Such scaling laws, that have been primarily derived to estimate impact-induced melting on Earth, are based on semi-analytical models (e.g., Grieve and Cintala 1992; Grieve and Cintala 1997; Croft 1982; Bjorkman and Holsapple 1987, Tonks and Melosh 1993) or simulations using shock-physics codes (e.g., O'Keefe and Ahrens 1977, Pierazzo et al 1997, Barr and Citron 2011). To estimate the amount of impact-induced melting, scaling laws usually do not account for pre-impact target material temperature (e.g., geothermal profiles), nor how lithostatic overburden pressure may affect melting. Thus they may not be applicable to impactors that are large enough to penetrate the base of the lithosphere. Previous studies investigated the effect of different thermal profiles on crater morphometry or mantle material exposure (e.g. Miljkovic et al. 2013, 2015, 2016) and ejecta thickness distribution (Zhu et al. 2017) but did not quantify melt production. Abramov et al. (2012) combined existing scaling laws (Bjorkman and Holsapple 1987; Pierazzo and Melosh 2000) and extended those by a correction factor adjusting the required melt energy E_m according to the temperature in the average depth of melting to roughly account for the temperature gradient in the targets. Tonks and Melosh (1993), using a simple analytical model, find significant differences in melt production for a giant impact forming a magma ocean on Mars depending on mantle temperature (T_0 = 1490 and 298 K). Marinova et al. (2011) studied melt production by giant impacts (L > ~ 400 km) on Mars considering a hot thermal profile and various impact angles using a smoothed particle hydrodynamic (SPH) code. However, they did not investigate the transition towards smaller impact events nor the contribution to the overall melt budget from decompression melting due to upwelling of initially deep-seated rocks. Ivanov and Melosh (2003) showed that decompression melting is effective for impactors larger than 20 km in diameter colliding with a hot, early Earth at a velocity of 15 km/s. Mars is best suitable to study impact-induced decompression melting since it is big enough to exhibit a sufficiently steep pressure and temperature gradient as indicated by its volcanic history (e.g. Robbins et al. 2011, Hartmann et al. 1999). In addition, a large number of ancient, basin-sized craters are preserved that can be studied. In summary, previous studies did not adequately consider the planet's thermal state and vertical material transport during the crater formation process on melt production and distribution over a wide range of impactor sizes. Our work aims at a better understanding of the impact-induced melt production on Mars throughout its early history, with implications on melt distribution and the overall cratering record.

In this paper we present a comprehensive set of simulations using the shock physics code iSALE covering a wide range of impact conditions on Mars. In particular, we focus on the effect of the temperature gradient of Mars and how it evolves over time. Further, we determine the degree of melting, the provenance of the melt, we seperate between shock and decompression melting and track the distribution of melt in our models to assess its effect on the final crater morphology.

2. Numerical modeling of impact-induced melt production:

2.1 Impact modeling:

We have used the iSALE (2D, Version Dellen) shock physics code (Amsden et al. 1980; Collins et al. 2004; Wünnemann et al. 2006) to quantify melt production, its provenance, and final distribution as a consequence of impacts on Mars. We employ a 2D cylindrical geometry for the computational grid which allows us to simulate vertical impacts only. We do not investigate the effect of the impact angle α_{imp}; thus, our melt estimates may be interpreted as an upper limit since the impact melt volume decreases with α_{imp} (see Section 4). We model spherical impactors resolved by 50 cells per projectile radius (50 CPPR). It has been shown that at this resolution iSALE underestimates the melt volume by less than *~10%* (Wünnemann et al. 2008). Relative to the expected variations in impact melt production as a function of projectile and target properties the error is small. Also note that in most previous studies on impact melt production (e.g., Pierazzo et al. 1997, Barr and Citron, 2011, Quintana et al. 2015) only the total volume of shock-melt was determined, which requires a computation time until the shock wave has sufficiently attenuated below the critical shock pressure for melting (see below). In our study we also investigate the final distribution of melt, which requires a much longer computation time. Therefore, we consider 50 CPPR as a good compromise between computation time and accuracy. We consider a spherical target to account for geometric effects which may be important for very large impactors (L >= 100 km).

Further, we assume thermodynamic target conditions appropriate for early Mars that do account for different crustal thicknesses and a thermal evolution that covers a timespan of 1000 Myr. We use the semi-analytical equation of state package ANEOS (Thompson and Lauson 1972, Melosh 2007) to describe the thermo-dynamical behavior of the basaltic crust (Pierazzo et al. 2005), the dunitic mantle and the impactor material (Benz et al. 1989), and the iron core. We do not account for differentiated impactors and assume homogeneous dunitic composition and constant initial temperature. Unlike in most previous studies (e.g., Pierazzo et al. 1997, Barr and Citron 2011, Quintana et al. 2015), we employ a material specific elastic-plastic constitutive model (Collins et al. 2004) to account for more realistic crater formation and material distribution at the final state. Material parameters are stated in Tab. A1. The rheological behavior of molten material is approximated by assuming a constant viscosity of $\eta=10^{10}$ *Pa s* (Potter et al. 2013).

2.2 Computing melt volumes:

Melting in impact events occurs due to (1) the increase in entropy as a consequence of shock compression (shock melting), (2) lithostatic uplift of material which is associated with a decrease of the melting temperature (decompression melting), and (3) plastic deformation which dissipates heat in the material. The latter is important for low-velocity impacts U < 10 km/s (Quintana et al. 2015, Kurosawa and Genda 2018, Emsenhuber et al. 2018) on brittle targets, but less important in high-velocity and large impacts (estimated in this study at impactor diameters *L* larger than or equal to 10 km, depending on the geothermal profile). The current study focuses on impactor sizes and velocities, for which most of the melt is generated at a depth ranging from a few tens to a few hundreds kilometers. At these depths, crustal and mantle materials are ductile due to thermal softening (Ohnaka, 1995). Thus, we consider the heat contribution from plastic work to be negligible. We follow the commonly used approach to quantify melt production in impact simulation (e.g., Pierazzo et al. 1997, Pierazzo and Melosh 2000, Artemieva and Lunine 2005, Wünnemann et al. 2008, Barr and Citron 2011), where the peak shock pressure is used to determine the increase in entropy upon compression and to derive the post-shock final temperatures. Alternatively, one can also use the temperatures computed by iSALE, which in contrast to the other method include heating due to plastic work. However, this approach is considered not to be suitable in this work for various reasons as discussed below. We use massless Lagrangian tracers to record the maximum shock pressure P_{peak} and the final (lithostatic) pressure P_{final} after displacement. Initially, one tracer is placed in the center of each computational cell. Each tracer represents the volume of material of the cell and tracks the displacement as a consequence of crater formation. Following Pierazzo et al. (1997), the peak shock pressure has to be in excess of a material specific, constant critical shock or melt pressure P_M, which corresponds to a certain melt energy E_M or entropy S_M, to cause melting after the release from shock pressure. This approach implies two assumptions, namely that the initial temperature is negligible and the material is unloaded from shock compression to standard conditions (atmospheric pressure). These assumptions are approximately valid for small impacts <= 10 km, but do not hold true for very large impacts, where crust and mantle materials are affected by the planetary temperature gradient and overburden hydrostatic pressure.

To determine the tracers' final temperature T_{final} we use the peak shock pressure P_{peak} recorded by each tracer in the iSALE simulations. Then, in a post processing step, we use ANEOS to calculate for a given tracer the release path from P_{peak} along an adiabat to the final lithostatic pressure P_{final} that is given by the depth where the tracer is finally located. Note, the Hugoniot curve and the release path depend on the initial P_0,T_0-values that are defined by the assumed geothermal profile. The thermodynamic path is illustrated in a P-T space in Fig. 1, where the initial state (P_0,T_0) is indicated by the thermal profile (thick black line). For five example tracers initially located at different depths (black triangles) the shock loading by ΔP = 60 GPa and adiabatic unloading path is shown. A tracer located initially close to the surface (I) is shocked along the Rayleigh line (thermodynamic path at the shock front calculated by ANEOS; red dash-dotted line) to the peak shock pressure (II) and subsequently unloads along an adiabat to the final lithostatic pressure (III). Note, the final lithostatic pressure P_{final} may be lower than the initial pressure due to lithostatic uplift upon crater collapse. Eventual decompression up to atmospheric pressure as a consequence of the upward transport of material in the course of crater formation is indicated by the dotted line in Fig. 1. If the final temperature T_{final} (III, diamond) is below the solidus $T_S(p)$ no melting occurs. For higher initial temperatures T_0 (black triangles) different Hugoniot curves (dashed lines) and release adiabats (thick colored lines) have to be considered. The final location between solidus and liquidus (thin black lines) defines the degree of melting. We assume that the fraction of melt, m_f, increases linearly with the temperature increase between solidus and liquidus; $m_f = (T_{final} - T_S) / (T_L - T_s)$, applicable for $T_{final} > T_S$ and $T_{final} < T_L$.

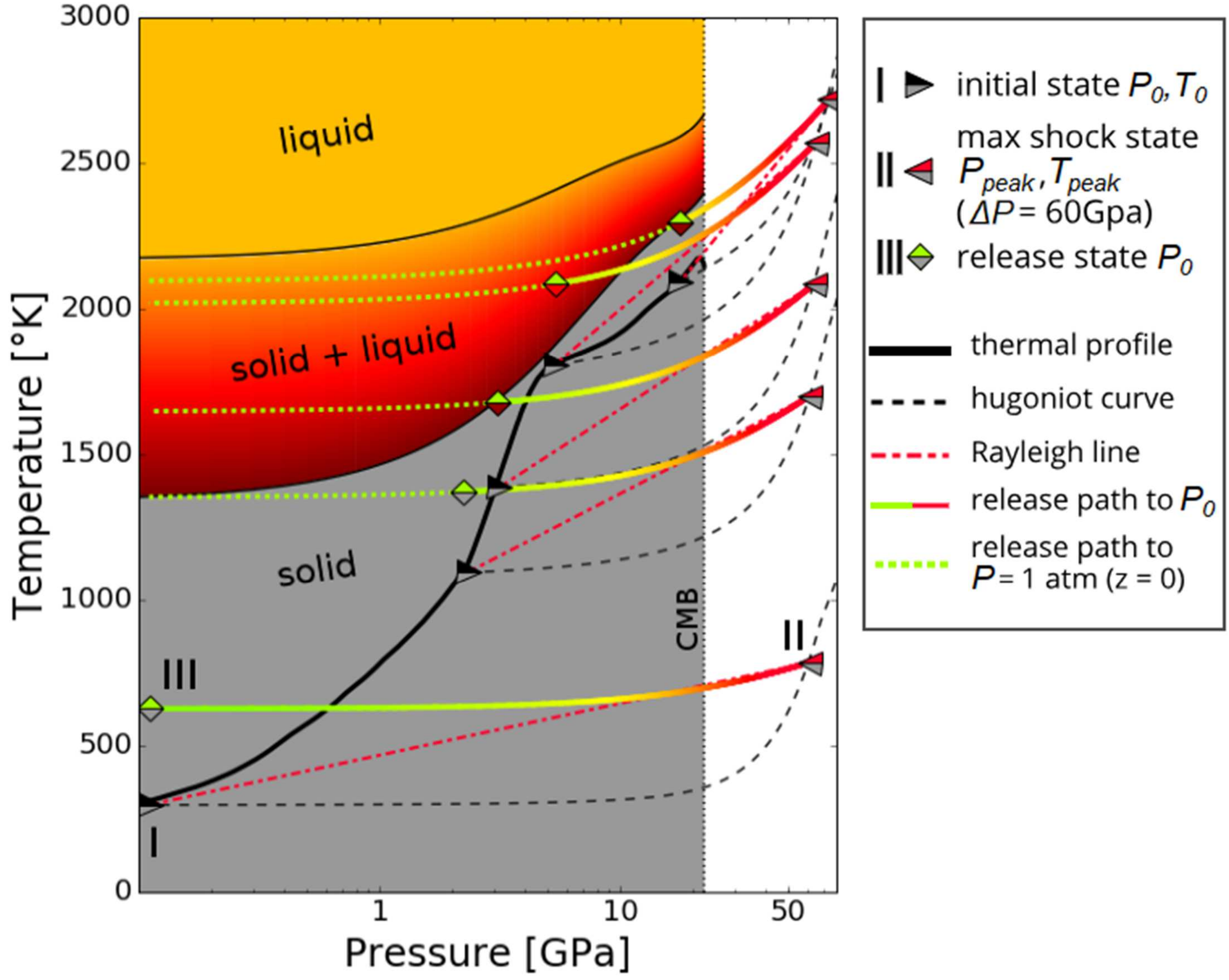

Figure 1: Thermodynamic paths upon shock and unloading for dunitic material with different initial conditions in temperature-pressure space. Different shock and release paths for $\Delta P = 60\ GPa$ are illustrated to demonstrate that melting of the material also depends on initial conditions and final release pressures P_{final}. The thermal profile (black line) describes an early Mars with a thin crust (T_{late}^{thin}, see 2.4). The initial state (I, black right facing triangles) is described by the thermal profile (thick black line) and is connected with the shock state (II, red left facing triangles) by the Rayleigh line (red dash-dotted line). The adiabatic release paths (colored line) end at the final stage (III) where diamonds indicate unloaded material to initial pressure. Further decompression up to atmospheric pressure is indicated by dotted lines. The solidus and liquidus curves (thin black lines) indicate whether the material is molten. Dashed lines illustrate the Hugoniot curves that depend on the initial state (P_0,T_0).

The solidus and liquidus curves shown in Fig. 1 are taken from literature (Ruedas and Breuer 2017, pers. communication Ruedas) to avoid inconsistencies with thermodynamic state models of martian interior evolution based on the chemico-physical cooling models. This improved post-processing procedure to determine melting from peak shock pressure accounts for both the initial target temperature and the final lithostatic pressure. To separate the two melting mechanisms, shock melting and decompression melting, we determine a parameter m_D that expresses the amount of decompression melting relative to all considered melting mechanisms $m_D = \Delta T_D / (\Delta T_D + \Delta T_{shock})$, where the temperature increase due to shock is given by $\Delta T_{shock} = T_{final}(P_{final}) - T_0(P_0)$ and the reduction of the melt temperature due to decreased lithostatic pressure can be calculated by $\Delta T_D = [(T_S\ (P_0) + T_L\ (P_0)) - ((T_S\ (P_{final}) + T_L\ (P_{final}))] / 2$. Finally, we determine the total amount of melt V_m by summing up the volume of partially to fully molten tracers using the volume of the cells where the tracers were initially located multiplied by the melt fraction m_f. Our method to determine melt production overcomes previous shortcomings regarding the pre-impact initial temperature and the contribution from decompression melting. However, it may overestimate shock heating if the peak shock pressure is achieved by multiple shock waves ramping-up the peak shock pressure. Since the major entropy increase is caused by the primary shock wave we consider this effect to be negligible. As mentioned above, we also neglect the contribution of plastic work. Both effects can be taken into consideration by using the final temperature in each individual cell that is calculated by iSALE. This method has been used in previous studies to determine the shock-induced heating and melting (e.g., Quintana et al. 2015). But this approach is not applicable here, as we include the late-stage crater modification processes where the temperature field is subject to significant numerical diffusion, which is intrinsic to the Eulerian advection scheme in iSALE (Collins et al. 2013), causing an artificial increase/decrease in the total melt volume.

2.3 Determination of the transient crater:

The transient crater describes the shape of the still-evolving cavity at the end of the excavation stage and the beginning of the crater collapse. The determination of the transient crater may be problematic for large impact events, because crater collapse occurs at different times and different places in the course of the crater formation along the cavity wall (e.g., see discussion in Elbeshausen et al., 2009). Thus, no specific point in time exists when the transient crater is fully developed and therefore, it cannot be straightforwardly measured at a single time step in numerical models. In previous studies on basin formation (e.g., Elbeshausen 2009, Prieur 2017, Potter 2012) the transient crater was often estimated by the size of the crater at the time when the maximum crater volume occurs; however, at this time the crater floor is usually already collapsed and a central uplift has formed. We determined the volume of the transient crater by tracking all grid cells throughout the excavation stage that are “empty” (cells with $\rho < 1000\ kg/m^3$) for at least one time step. The added volume of all empty cells corresponds to the volume of the transient crater (cf. Fig. 8 blue dashed lines). To correct for numerical inaccuracies near the crater rim, where additional empty cells appear in the course of the modification stage, we fit the transient crater with a paraboloid of higher order while excluding the rim zones (cf. Fig. 8 black dashed lines).

2.4 Model setup:

We carried out a suite of more than 100 impact simulations and systematically explored melt production and distribution. We varied the impactor diameter L over three orders of magnitude from *1* to *1000 km* and considered impactor velocities U of *10, 15,* and *20 km/s.* Impact events on a smaller scale L < 10 km are considered to compare with previous work.
We consider two thermal profiles to approximate varying geothermal conditions of an early Mars, and two crustal thicknesses. The temperature profiles are taken from mantle convection

models by Plesa et al. (2016). Figure 2 illustrates the thermal profiles for the different cases. Additionally, the solidus (Ruedas and Breuer, 2017) and liquidus curves (pers. communication Ruedas) are plotted. Cases T_{early}^{thin} and T_{early}^{thick} represent temperature profiles for a very early state of Mars (~*4.5 Ga,* red lines) and cases T_{late}^{thin} and T_{late}^{thick} represent late state temperature profiles after 1 Ga cooling history (~*3.5 Ga,* blue lines).

Crustal thickness varies from 45 (thin) to 87 km (thick), respectively, roughly corresponding to Martian low- and highlands. The core-mantle boundary (CMB) is fixed at a depth of *1700 km*. For the individual thermal profiles, the thickness of the apical conductive thermal boundary is illustrated by dashed lines and measured at d_L = 61.2 km (T_{early}^{thin}), d_L = 322.9 km (T_{early}^{thick}), d_L = 64.3 km (T_{late}^{thin}) and d_L = 142.6 km (T_{late}^{thick}). Note that in the following we refer to this parameter as lithosphere thickness for simplicity; however, strictly speaking it does not mark a rheological but a thermal boundary. For a list of parameters that have been used to generate the thermal models, we refer the reader to the study of Plesa et al., (2016). For the case employing an average crustal thickness of 45 km (T^{thin}cases) the pressure-dependence of the viscosity is higher than for the T^{thick} scenarios (average crustal thickness of 87 km), leading to a less efficient heat transport in the former compared to the later cases. In addition, for the thin crust scenario, more heat producing elements are located in the mantle compared to the thick crust scenario. This leads to a higher temperature in the sublithospheric mantle for the T_{late}^{thin} case compared to the T_{late}^{thick} case (cf. Fig. 2a and 2b). The chosen range of initial thermal conditions of Mars allows us to estimate melt production over a wide range of possible Mars scenarios including the early thermal evolution history of Mars. We also note that hydrostatic equilibrium in the setup is achieved by iteratively adjusting density, pressures, and gravity according to the thermal profiles. After calculating the planet's gravity profile in the beginning of a simulation, it is assumed to be constant.

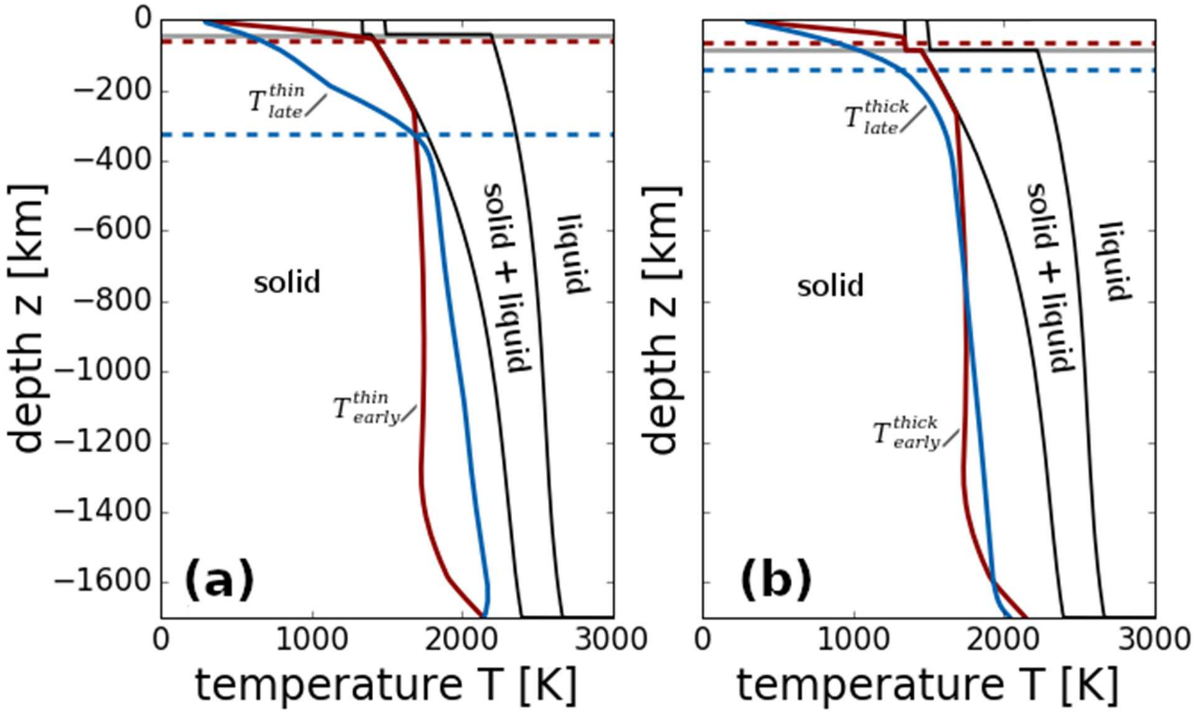

Figure 2: Thermal profiles for an early and late Mars (Plesa et al. 2016). Different cases with varying crustal thickness and thermal profiles are shown (see text). The crust mantle interface is marked by a grey line and the apical thermal boundary layers (bottom of the lithosphere) d_L are illustrated by dashed lines. a) and b) indicate thin and thick crust cases, respectively.

3 Results:

3.1 Melting of preheated and compressed material:

Impact-melt generation is often estimated by scaling laws that relate melt volume with the so-called melt number (U^2/E_M) (e.g., Pierazzo et al. 1997, Barr and Citron 2011, Quintana et al. 2015, Bjorkman and Holsapple 1987), where U is the impact velocity and E_M the specific melt energy of the Rankine-Hugoniot or shock state from which isentropic release ends at the 1 atm on the liquidus. E_M is directly proportional to a critical shock pressure for melting P_M or entropy S_M (see section 2). As discussed above this approach does not account for the fact that lower shock pressures are required to melt relatively warm and compressed material. In addition, decompression melting may significantly contribute to the melt production. In our approach, the critical shock pressure P_M is a function of the final pressure P_{final} and depth and depends on the assumed thermal profile and crustal thickness. Figure 3 indicates how the thermal profiles affect the material's tendency to shock and decompression melting with varying depth. In particular, the figure shows how the critical shock pressure for 1% melt fraction ($P_{1\%}$ for $m_f = 0.01$) and complete melting (P_M for $m_f = 1.0$), changes after releasing to the initial overburden pressure P_0 (black solid and dashed line, respectively). To address decompression melting, the green line in Fig. 3 indicates how much structural uplift Δz_{up} of material initially located at a certain depth is required to enable incipient decompression melting. The green area indicates possible decompression melting to a higher degree until the maximum possible uplift distance is reached, which is limited by the uplift to the surface $\Delta z_{up} = -z_0$. For all cases shock melting occurs close to the surface at a shock pressure of $P_{1\%}$ ≈ 50 and P_M ≈ 65 GPa, for the basaltic crust which is in agreement with experimental data (e.g., Stöffler et al. 2018). However, with increasing depth the critical shock pressures P_M and $P_{1\%}$ for the different thermal profiles and crustal thicknesses differ significantly. For instance, for an early Mars with a crustal thickness of 45 km (T_{early}^{thin}, Fig. 3a), the shock pressures decrease with depth to 19.8 and 25.8 GPa for $P_{1\%}$ and P_M, respectively, at the crust-mantle boundary. Due to the different material in the mantle there is a sharp increase in $P_{1\%}$ and P_M to 51.2 and 109.3 GPa, respectively. In the upper ~20 km of the mantle $P_{1\%}$ decreases until the depth of the lithosphere (dashed horizontal line) is reached, followed by a depth range of about 200 km where P_M is almost constant, before it increases again. P_M is almost constant in the upper few hundred kilometers and decreases slightly with increasing depth. Comparing the different thermal states shows that the variations of P_M and $P_{1\%}$ with depth depends on the geothermal profile. In a depth range from the bottom of the lithosphere d_L (dashed horizontal lines) and further down, where the thermal profile approaches the solidus, the critical pressure for melting is reduced. In turn, where the initial temperature at a certain depth is much lower than the solidus T_S, high shock pressures P_{peak} are required for melting. The red and yellow area indicates critical shock pressures that result in partial melting above m_f > 0.01 and complete melting (m_f = 1., super heated material) respectively. A similar behavior can be observed for the distance $\Delta z_{up\text{-}M}$ (m_f > 0) to which unshocked material needs to be uplifted for incipient decompression melting. This critical uplift distance (green line), however, is limited by the maximum possible uplift to the surface $\Delta z_{up\text{-}max} = z_0$ (indicated by the green dotted line), which is equivalent to complete unloading from the initial lithostatic overburden pressure to atmospheric pressure. The shallowest or minimal depth from which the material experiences pure decompression melting when uplifted to the surface is at z_{min}= 50 - 240 km (Fig.3). It varies due to target structure and geothermal profile. The variations of the melt pressures P_M and uplift distances $\Delta z_{up\text{-}M}$ with depth between the different thermal states shown in Fig. 3 indicate that strong differences in shock and decompression melting can be expected for the early and late Mars cases (~4.5 vs 3.5 Ga).

Figure 3: Depth-profiles of critical peak shock pressures $P_{1\%}$ (m_f = 0.01) and P_M (complete melting, m_f = 1) are illustrated with a solid and dashed black line, respectively. The plots are

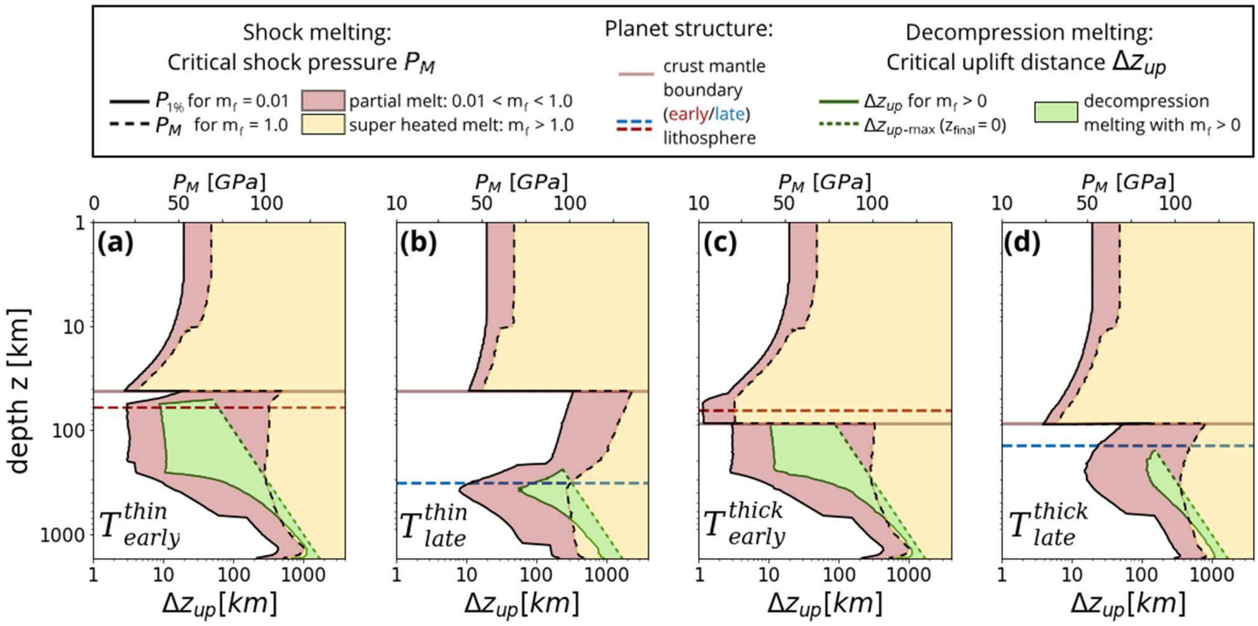

for an early (a,c) and late (b,d) Mars with a thin (a,b) and thick (c,d) crust. The red and yellow area indicates critical shock pressures that result in partial melting above m_f > 0.01 and complete melting, respectively. For the shock heated material ($P_{1\%}$ and P_M) we assume that the material is unloaded to the initial lithostatic pressure. Red and blue horizontal dashed lines indicate the lithosphere thickness d_L. Furthermore, uplift distances $\Delta z_{up\text{-}M}$ that are required for incipient decompression melting ($m_f > 0$) for unshocked material are illustrated by a green line. The green area indicates possible decompression melting to a higher degree up to the maximal possible uplift distance $\Delta z_{up\text{-}max} = z_0$ (green dashed line).

3.2 Comparison with scaling laws:

In a first step, we compare the result of our modeling study with melt volumes calculated according to the parameterization in Abramov et al. (2012) for basalt and Pierazzo et al. (1997) for dunite:

$$log(M_V) = a + 3/2\ \mu\ log\ (U^2/E_M) \qquad \text{(Eq. 1)}$$

M_V describes the melt efficiency, which is defined by the melt volume V_M normalized by the projectile volume V_{proj} ($M_V = V_M/V_{proj}$). The scaling parameters $a = -0.8$ and $\mu = 0.701$ are stated in Pierazzo et al. (1997). The specific melt energy E_M is adjusted to ensure that the isentropic release for the shock state ends at the 1 atm point on the liquidus (or solidus for E_S) for the given equation of state and melt temperatures T_L (and T_S, cf. A1). Note that in these scaling laws the specific melt energy E_M is assumed to be constant. Accordingly, the melt efficiency is a constant value that depends only on the impact velocity and the lithology of the target. Figure 4 shows the melt efficiency M_V as a function of impactor diameter L, for an impact velocity of U=15 km/s. According to the scaling law (Eq. 1) the melt efficiency for basalt is larger than for dunite (c.f. Tab. 1). First we carried out simulations to determine melt efficiency for the same conditions assumed in scaling laws, where temperature T_0, pressure P_0, and thus, E_M are constant and depth independent. We mimic such conditions by assuming zero gravity in our models and set the initial target and projectile temperature to T_0 = 297 K. If we neglect strength and assume hydrodynamic behavior of the target material, our simulations (Fig. 4; red triangles and blue upside-down triangles for basalt and dunite, respectively) agree very well with the calculated melt efficiencies from scaling laws and are within 7.4% and 18% for basalt and dunite respectively. The small shift can be explained by adjusting the melt energy E_M, differences in the codes or numerical resolution compared to Pierazzo et al. (1997) and Barr and Citron (2011) for dunite (black dotted line). Similar conclusions hold true for models in this study and the calculated melt efficiency using parameters stated by Abramov et al. (2012) for basalt (black dashed-dotted line for small scale impactors). If considering strength (cf. A1), the melt production slightly decreases (triangles on dotted lines, Fig. 4) by 13.3% and 51.2% for basalt and dunite, respectively. This reduction can be explained by a faster shock wave decay due to material strength (Bierhaus et al., 2013). We also note that the effect of material strength is reduced when assuming larger impactors $L >= 10$ km, where the material strength becomes negligible at a certain depth due to thermal softening as a consequence of the hot planet interior. Next, we account for a layered structure of the target composed of a basaltic crust and dunitic mantle. As before, we assume two different martian crustal thicknesses, 45 and 87 km. For small impactor diameters the simulated melt ratios follow the line for pure basalt targets as melt is only generated in the crust (green diamonds). For impactor diameters $L > 10$ and $L > 30$ km, for case T^{thin} and T^{thick}, respectively, the melt efficiency decreases, and approaches the line for pure dunite for $L > 100$ and $L > 300$ km, respectively. The larger the impactor the more melt is generated in the mantle until the total melt volume is dominated by mantle melting. In the following, we use these simplified scenarios as reference cases representing scaling law predictions for a layered target.

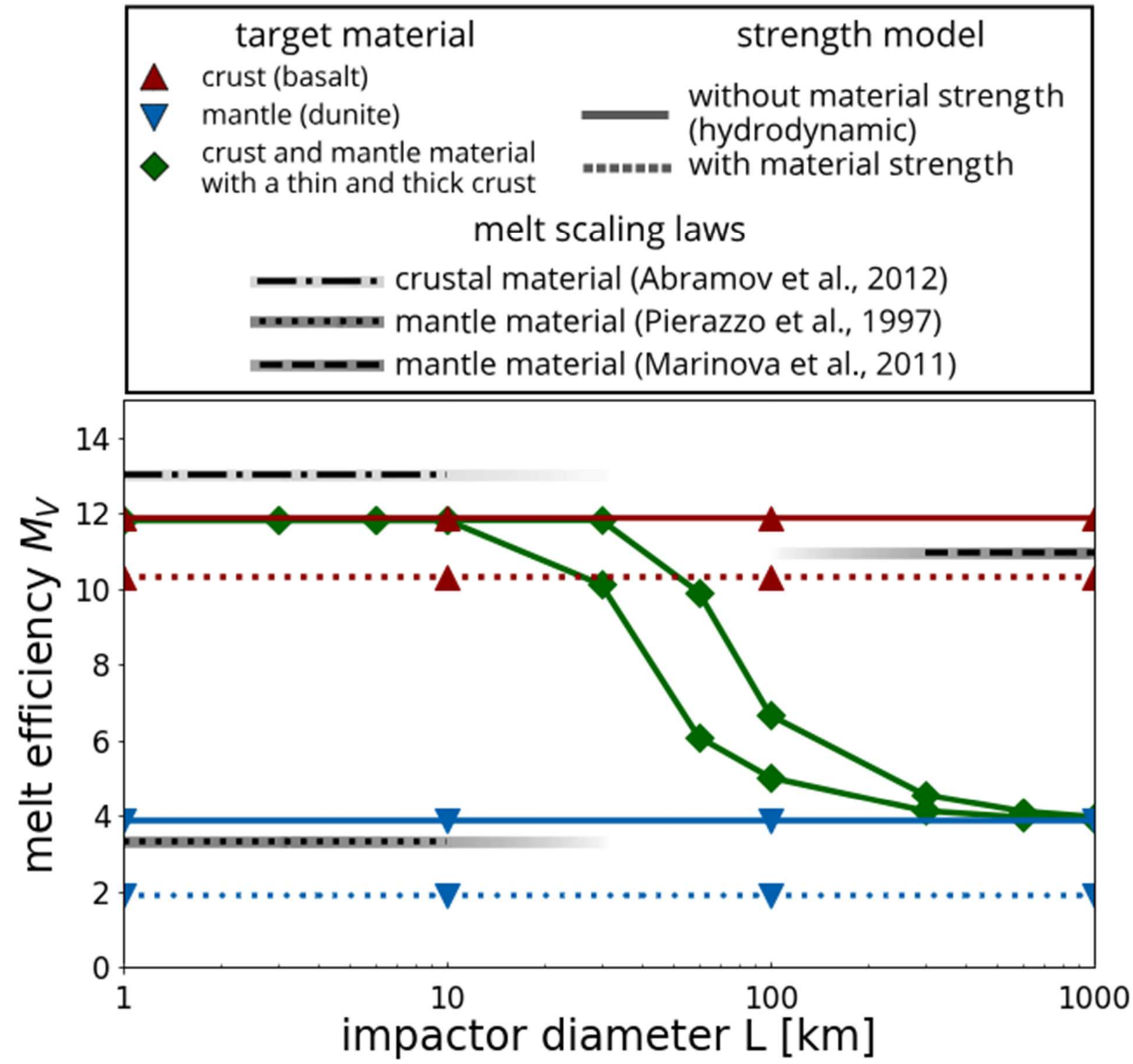

Figure 4.: Melt efficiency $M_V = V_M/V_{proj}$ as a function of impactor size at an impact velocity of 15 km/s. The black dash-dotted line illustrates melt efficiency derived by scaling-laws for crust material (Abramov et al. 2012). The black dotted line illustrates scaling laws for mantle material applicable for small scale impactors (L 10 km, Pierazzo et al. 1997) under "normal" conditions and the dashed line for large-scale impactors (L 300 km, Marinova et al. 2011) derived by simulations with preheated and pressurized rocks. Triangles represent results from simulations for purely basaltic (up) and dunitic (down) targets with (on dotted line) and without (on solid line) considering material strength. Green lines (diamonds) represent the two layered cases with different crustal thicknesses (45 and 87 km, respectively) and are considered as reference cases.

3.3 Total melt production by impacts in Martian history:

Our results for melt efficiency $M_V = V_M/V_{proj}$ are shown in Fig. 5 as a function of impactor size for the four different thermal profiles and 15 km/s. In our simulations, we took into account melt production by shock heating and decompression as a consequence of structural uplift. The red line indicates melt production on an early Mars (T_{early}) and the blue line after 1 Gyr of cooling history (T_{late}) for a thinner (Fig. 5a) and thicker (Fig. 5b) crust. The green line represents the reference case (see previous section), where the effects by an increasing temperature in the subsurface and decompression are neglected.

The dashed vertical line indicates the impactor size *L* for which most of the impact energy is deposited at the base of the lithosphere. This depth approximately corresponds to the so-called equivalent depth of burst d_B, which can be estimated by the diameter of the impactor if the density ratio of impactor and target is close to one ($d_B = L\ (\rho_{proj}/\rho_{target})^{0.5}$; Melosh 1989, chapter 7.3).

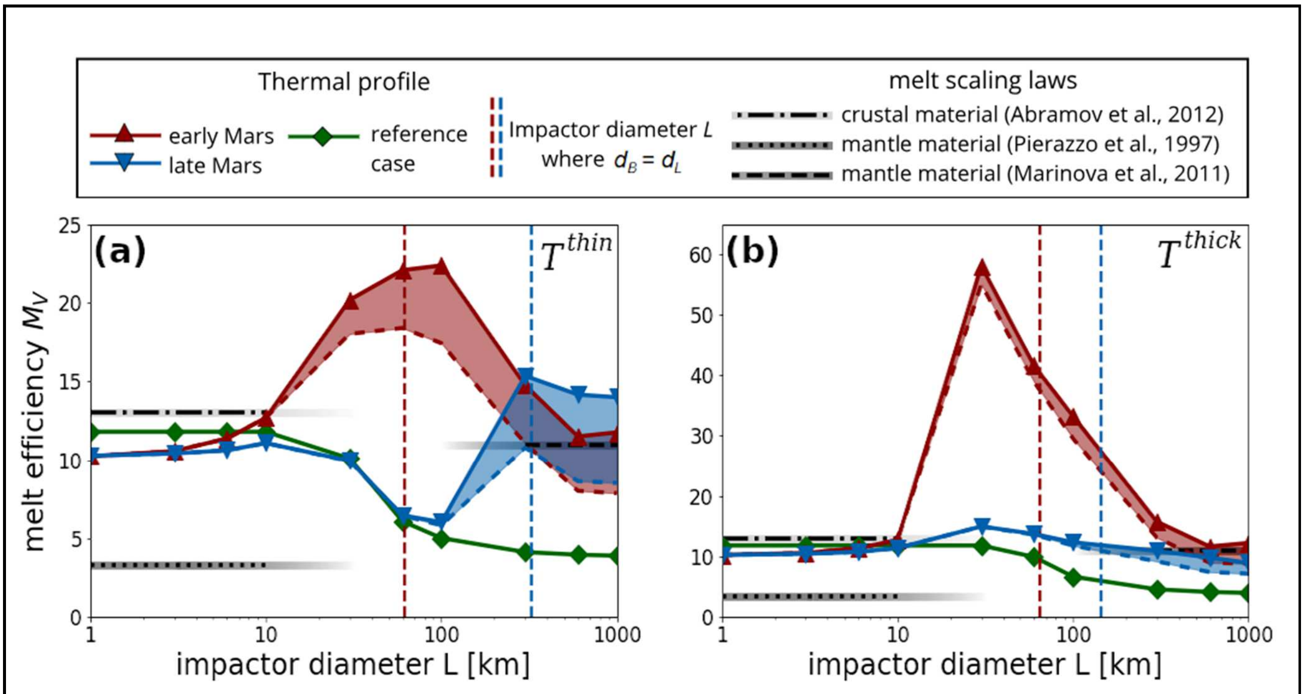

Figure 5.: Melt efficiency M_V ($M_V = V_M/V_{proj}$) as a function of impactor size for an early (red, ~4.5 Ga) and late (blue, ~3.5 Ga) Mars for different crustal thicknesses T^{thin}(a) and T^{thick}(b) at 15 km/s. Scaling-laws for crust material (black dash-dotted line, Abramov et al., 2012), mantle material (black dotted line; L □ 10 km: Pierazzo et al., 1997, black dashed line L □ 300 km: Marinova et al., 2011, c.f. Fig 4.) and the reference case (green) are plotted for comparison. Colored areas indicate the fraction of decompression melting of the total melt. The vertical dashed lines indicate at which impactor size *L* the most energy is deposited at the base of the lithosphere $d_B = d_L$ for each thermal profile (red = early, blue = late).

For small impactor diameters, L < 10 km, melt efficiencies M_V are very similar for all cases and close to the reference case (deviations are due to material strength, see previous section). Melt is primarily generated in the basaltic crust. With increasing impactor diameter *L,* the melt efficiency M_V increases with a maximum at L = 100 km and L = 30 km for an early Mars (red line) for a thin (Fig. 5a) and thick (Fig. 5b) crust, respectively. The increase in melt efficiency

M_V corresponds to the increased equivalent depth of burst d_B which approaches the base of the lithosphere d_L. Close to d_L shock melting is most effective due to the relatively low melt pressures P_M. However, melt pressures are not necessarily the lowest at the depth of the lithosphere d_L since they are further affected by material specific melt temperatures (cf. Figs. 3 and 8). Thus, the maximum of melt efficiency M_V may not occur exactly where the equivalent depth of burst is equal to the depth of lithosphere $d_B = d_L$ (Fig. 5b). Also decompression melting can significantly affect melt efficiency with increasing d_B. In the extreme case, the melt volume is almost an order of magnitude larger than suggested by scaling laws and the reference case. The increase is less pronounced for the colder target conditions (blue line, T_{late}) and occurs at larger impactor diameters (L = 300, 30 km for thin and thick crust, respectively). For very large impactors (L > 100 km) the melt efficiency decreases; except for the cold scenario with a thin crust (blue line, Fig. 5a), where the maximum in melt production occurs at larger impactor diameters (L = 300 km) and remains then almost constant. This is due to the the fact that the deep mantle is relatively hot in this target scenario (cf. Fig 2a). For very large impactors (L > ~500 km), we compare our results with a scaling-law derived by SPH simulations (Marinova et al., 2011) that account for pressure dependent melt energy E_M and a hot planet interior. The scaling-law is valid for head-on collisions (α_{imp} = 90°) and assumes velocity dependent melt efficiency of $M_V = 0.075\ U^{1.84}$ (black dashed line for large scale impactors). We note that the SPH simulations are based on a Tillotson equation of state for olivine. However, despite this difference, we find that the melt production is in agreement with the scaled results from Marinova et al. (2011) for large scale impacts.

3.4 Decompression vs. shock melting:

It is expected that decompression melting contributes significantly to the total melt volume in large impacts, as more material from greater depth is stratigraphically uplifted with increasing impactor size. We find that decompression melting has a significant effect on melt production for specific combinations of impactor sizes and geotherms. In Fig. 5 the shaded areas illustrate the portion of decompression melting on the total melt production for the early and late Mars cases. With larger impactor size, deeper seated material can be stratigraphically uplifted until the shallowest (minimum) depth $z_{up\text{-}min}$ is reached, where incipient decompression melting is possible if the material is fully uplifted to the surface (c.f. Fig. 3). We approximate the distance to which material is possibly uplifted within the crater by the depth of transient crater d_{tc}. The smallest impactor diameter L_D where decompression melting is possible is approximated if the transient crater depth d_{tc} is equal to the shallowest possible decompression melting depth $z_{up\text{-}min}$ and calculated at L_D = 14.8 km (T_{early}^{thin}), L_D = 93.8 km (T_{late}^{thin}), L_D = 25.4 km (T_{early}^{thick}) and L_D = 67.6 km (T_{late}^{thick}), respectively. These estimated diameters are in agreement with the occurrence of decompression melting for the different geotherm (c.f. Fig. 5). In comparison, Ivanov and Melosh (2003) found that, on Earth, a 20 km-diameter impactor with a velocity of 15 km/s is not sufficient to cause decompression melting L_D > 20 km. Furthermore, they found that material needs to be uplifted from 54 and 125 km depth for a hot and a cold geotherm, respectively, in order to cause decompression melting. In agreement with this work, we find that for impacts at 15 km/s decompression melting requires a similar minimum depth $z_{up\text{-}min}$ of at least 50 (T_{early}^{thin}) to 240 (T_{early}^{thick}) km, roughly corresponding to the thickness of the lithosphere (c.f. Fig. 3). These results indicate that in addition to possible material uplift (controlled mainly by impactor diameter and impact velocity), the depth of the lithosphere d_L (controlled by the geotherm) has an important effect on decompression melting. In this study decompression melting is most pronounced for a late Mars T_{late}^{thin} where it can be as high as 40% of the total melt volume (c.f. Fig. 5a). This might seem surprising since the geotherms for early Mars T_{early} appear to show lower uplift distances Δz and minimal decompression melting depth $z_{up\text{-}min}$. However, melting is mainly a combination of decompression and shock melting and in areas of very low uplift distances Δz, also the melt pressures P_M are low (c.f. fig. 3a,c). In these areas, melting is mostly due to shock heating. Furthermore, we find that decompression melting is most dominant when deep seated, moderately warm material is uplifted since the uplifted material is compressed adiabatically while the melt entropy $S_M(z)$ changes with depth. Thus, when uplifted from greater depth the material is likely to melt to a higher degree than from shallow depth. Compared to the other geotherms, T_{late}^{thin} has a relatively hot deeper mantle which results in significant decompression melting (e.g., T_{late}^{thick} it is at most 20%).

As an example, Fig. 6 shows the effect of decompression melting for late Mars with thin crust T_{late}^{thin} and impactor diameters L = 600 km (Fig. 6a) and L = 100 km (Fig. 6b). For both scenarios, the final melt distribution (right-hand side) and the initial material distribution (left-hand side) is plotted. In the upper two panels (a,b), colored material indicates molten materials, from shock melting (red) to decompression melting (green). The bottom panels (c,d) indicate the melt fraction of the material. As pointed out before, impactors with L = 100 km are barely large enough to produce pure decompression melting on a late Mars. Although small fractions of melt produced by a combination of shock heating and decompression are present, the contribution of decompression melting to the total amount of melt is negligible (d). For a larger impactor L = 600 km, decompression melting has a significant effect on melt production (a,c).

Figure 6: Provenance and final position of decompression melt for an L = 600 km (a) and L =

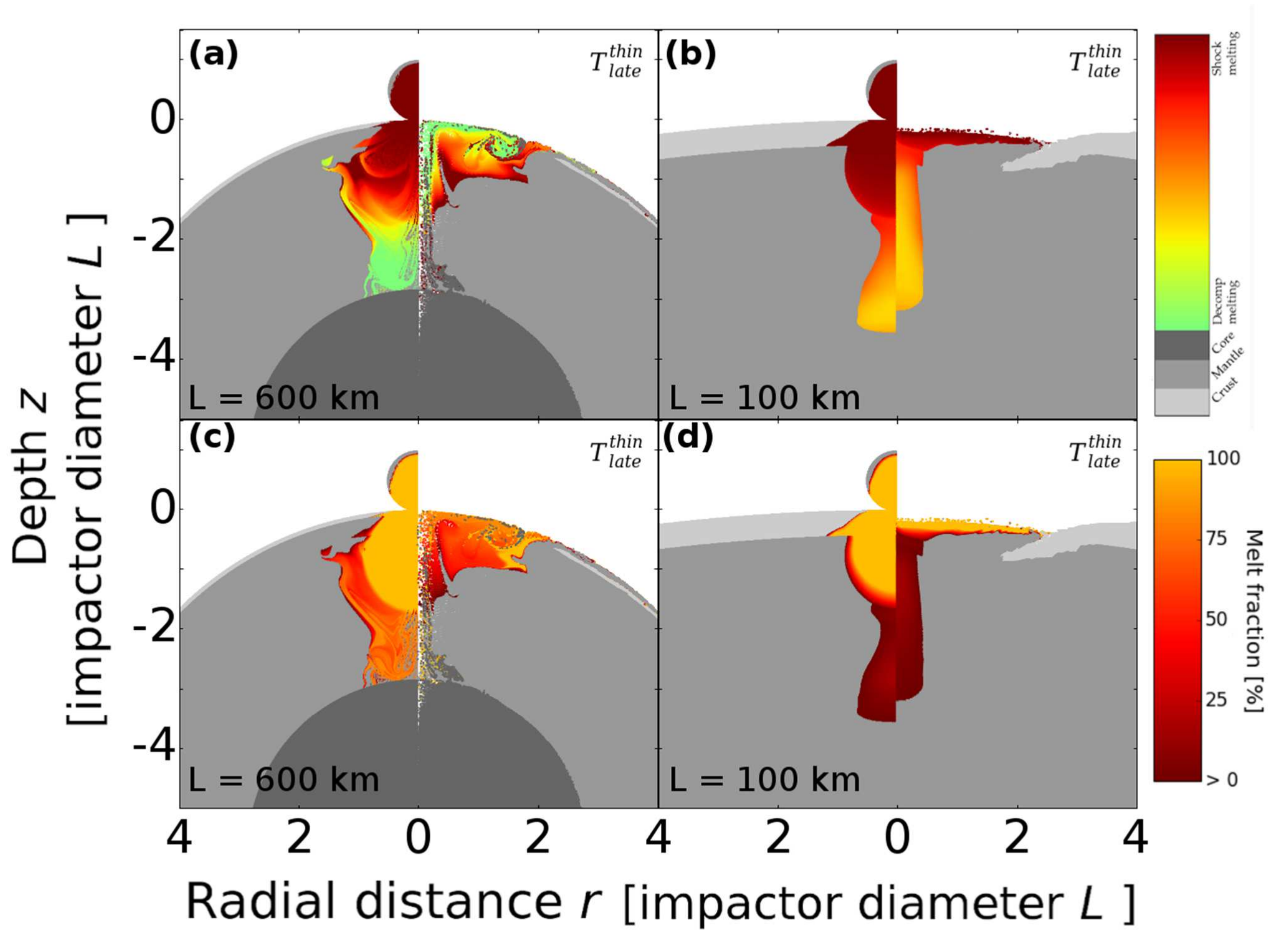

100 km (b) impact event for a late Mars-like planet T_{late}^{thin}. The melt fraction corresponding to panels (a) and (b) is shown in panels (c) and (d), respectively. For each case, the final distribution of melt is illustrated on the right-hand side of the panel and on the left-hand side the initial position of material and thus the provenance of melt is displayed. In panels (a) and (b) the colors indicate whether decompression (green) or shock (red) melting dominates, while in panels (c) and (d) red illustrates incipient and yellow complete melting. Different shades of greys represent solid material.

3.5 *The effect of velocity:*

Impact velocity has an important effect on target melting. Figure 7 illustrates the normalized melt production for different impactor diameters *L* and velocities for early and late Mars with a thin (a) and thick (b) crust. As expected, the higher the impact velocity the more melt is produced. This effect is in agreement with scaling laws for small scale impacts that only penetrate into crustal material (Abramov et al. 2012) and on planetary scale collisions where mostly deep seated, hot mantle material is involved (Marinova et al. 2011). The shape of the melt production curve is roughly independent of impactor size. Impact velocity causes a vertical shift of the curves and for higher velocities the peak in melt production is more pronounced, although the ratio between maximum and minimum remains approximately constant. Note that the range of impact velocity relevant for Mars' first billion years of evolution is from about 10 to 15 km/s (Raymond et al 2013).

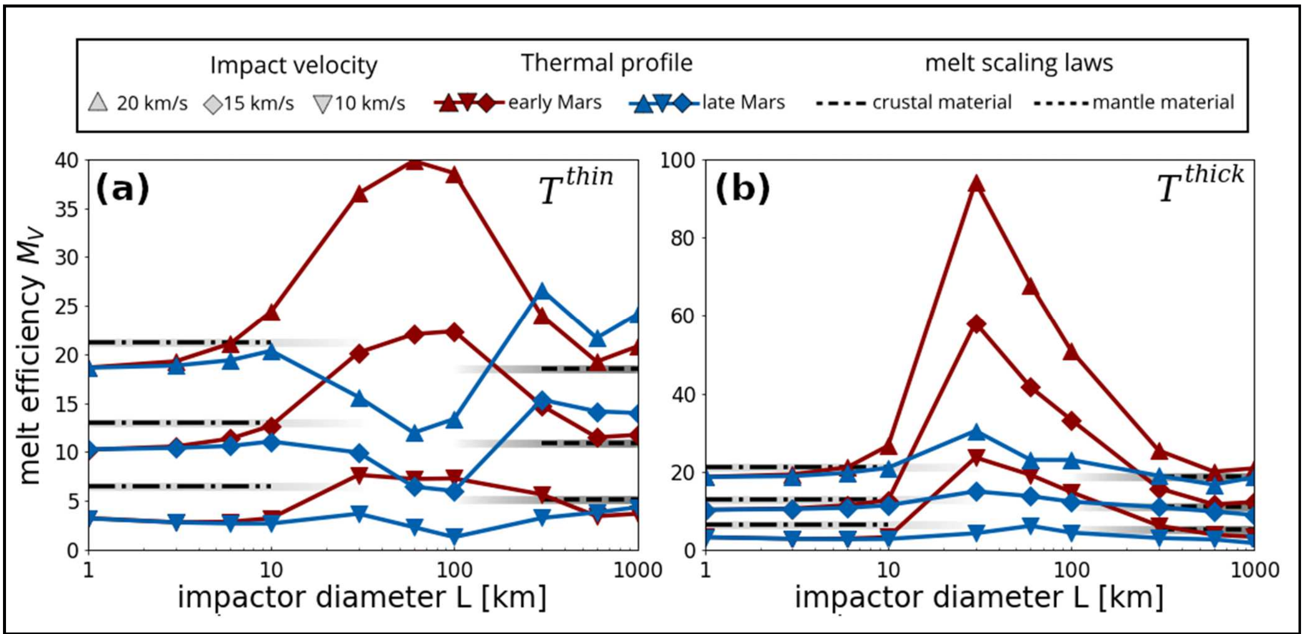

Figure 7: Melt efficiency ($M_V = V_{melt}/V_{proj}$) as a function of impactor size for different impact velocities (10 km/s: downward triangles; 15 km/s: diamonds, 20 km/s upward triangles) for early (red) and late (blue) Mars with a thin (a) and thick (b) crust. Scaling laws are illustrated for crust material under "normal" conditions applicable for small scale impacts L □ 10 km (dash-dotted line, Abramov et al. 2012) and mantle material under pressurized and preheated conditions applicable for large scale impacts L □ 300 km (dashed line, Marinova et al. 2011).

3.6 Provenance and distribution of melt:

Finally, we investigate the final distribution of melt, its provenance, and the morphology of the transient and final craters. Figure 8 shows results for impactor diameters L = 30 - 300 km (I-IV) and an impact velocity of 15 km/s for all geothermal profiles (a-d). All frames show the degree of partial melting (yellow indicates complete melting, red the onset of melting). The final distribution of melt is illustrated on the right-hand side and the panel on the left-hand side depicts the initial position of material. The latter illustrates the provenance of melting.

In the provenance-plot (left-hand panel) the almost spherical yellow region (complete melting) corresponds to the so-called isobaric core (e.g., Pierazzo et al., 1997), where shock pressure is almost constant and small attenuation occurs mostly due to geometric spreading. Its center is located in the equivalent depth of burst d_B. The extent of the complete melting area relative to the size of the impactor decreases with impactor size (compare top frame with bottom frame). The spherical geometry is distorted at the crust-mantle boundary due to the strong contrast in critical shock pressure for melting between crustal and mantle material. Beyond the isobaric core for a late Mars and impactor diameters L < 100 km (b,d, I-II) the fraction of melting decreases rapidly due to the fast decay of the shock wave from the critical pressure for complete melting P_M to the critical shock pressure for the onset of melting P_S. In these cases, decompression melting does not contribute to the total melt volume significantly (see Fig. 5). In all other cases decompression melting in addition to shock melting is not negligible and the zone, where partial melting occurs, reaches a much larger depth and lateral extent. This is most pronounced for an early Mars (first and third column).

Note, due to the usage of tracers, numerical diffusion, which tends to be problematic when tracking melt during the entire course of crater formation, is negligible and not an issue in our models. We stress that in all cases almost the entire completely molten and superheated material ends up near the surface forming a large melt pool. The zone of partial melting is less affected by the late-stage crater formation processes. It has been shown that large amounts of partial, deep-seated, melt can become buoyant and rise to the surface over time scales longer than covered by the impact simulations (e.g., Roberts and Arkani-Hamed, 2014; O'Neill et al. 2017; Ruedas and Breuer 2017, Padovan et al., 2017). Upon rising the percentage of partial melting would increase due to further decompression. However, quantification of this process is beyond the scope of this study. The final distribution of melt as shown in our simulations raises the question to what extent the final crater structures are flooded by uplifted melt. We note that our models do not aim at an accurate reproduction of crater morphology due to our limited resolution ($\Delta r = \Delta z = 0.01\ L$).This resolution is too coarse to unambiguously determine the thickness of melt layers and, thus, whether flooding of a given crater occurs. We also note that acoustic fluidization (e.g., Melosh 1979, Melosh & Ivanov, 1999) was neglected in our simulations, which results in unrealistic deep final crater structures for small impactors (roughly L =< 10 km). For very large impactors acoustic fluidization is less important and material strength is dominated by thermal weakening (as discussed previously in section 3.2).

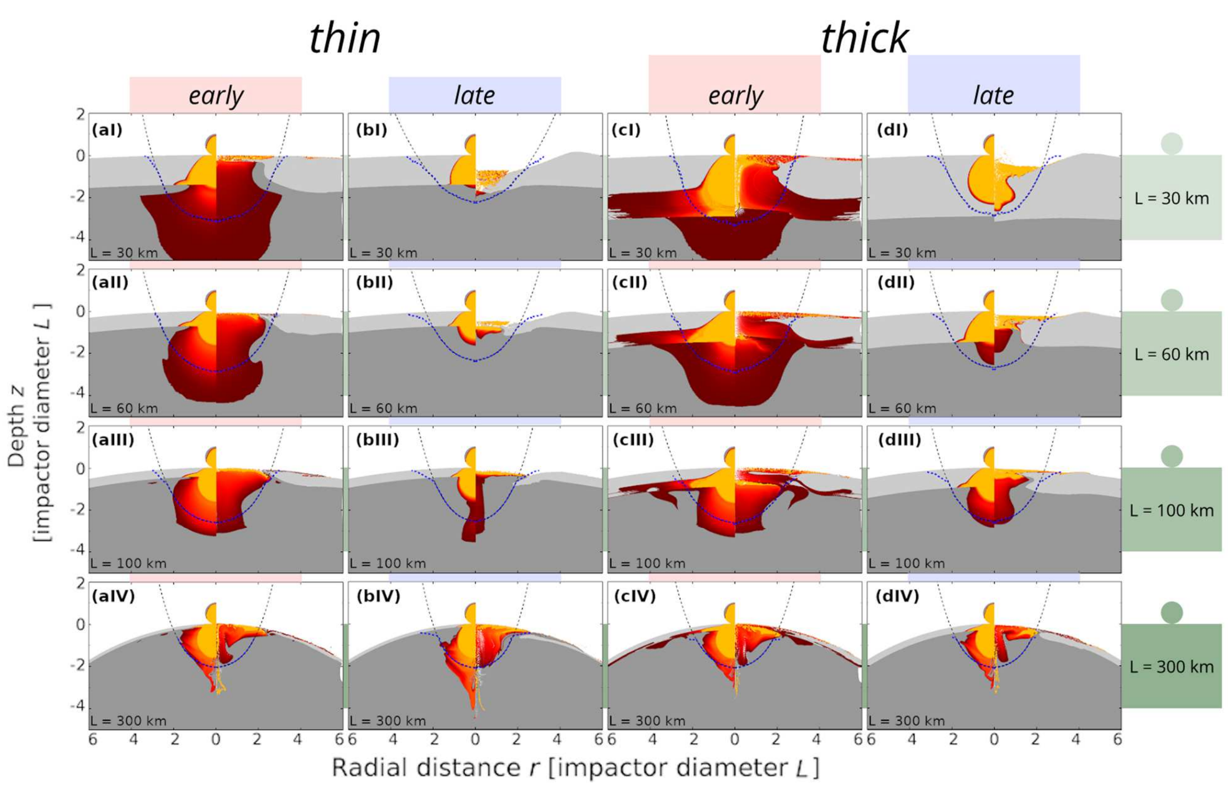

Figure 8: Provenance and final location of melt for different impactor sizes *(L* = 30 – 300 km, I-IV) for all geothermal profiles (a-d). The left panel shows the material provenance, and the right panel the final distribution of melt. The colors indicate the degree of melting where yellow represents complete and dark red incipient melting. Dashed lines indicate the measured transient crater (blue) and a paraboloid fit (black) to account for near rim inaccuracies (see section 2.4). Shades of grey indicate solid material, where lighter grey represents crustal and the darker grey mantle.

To estimate whether craters under certain circumstances may be entirely filled by melt one can compare the resulting melt volume V_M with the volume of the transient crater V_{tc}, where the latter is known to be larger than the final crater volume V. In this case, we normalize V_m and V_{tc} by the projectile volume V_{proj} which results in the efficiency $M_V = V_M / V_{proj}$ and the cratering efficiency $\pi_V = V_{tc} / V_{proj}$ (for $\rho_{target} = \rho_{proj}$). According to scaling laws at constant velocity *U* and gravity, the cratering efficiency π_V is a power-law of the impactor size *L* (e.g., Holsapple 1993, Elberhausen 2009), while the melt efficiency M_V is a constant (see section 3.2). Based on such scaling laws previous studies predict that the melt volume exceeds the volume of the transient crater volume for an impact velocity of 20 - 25 km/s and a transient crater diameter of 300 - 400 km for the Earth and 1800 km for the Moon (e.g., Tonks and Melosh, 1993, Grieve and Cintala, 1997). Our models allow for more accurate estimates as we also account for decompression melting and the thermal profile as a function of time.

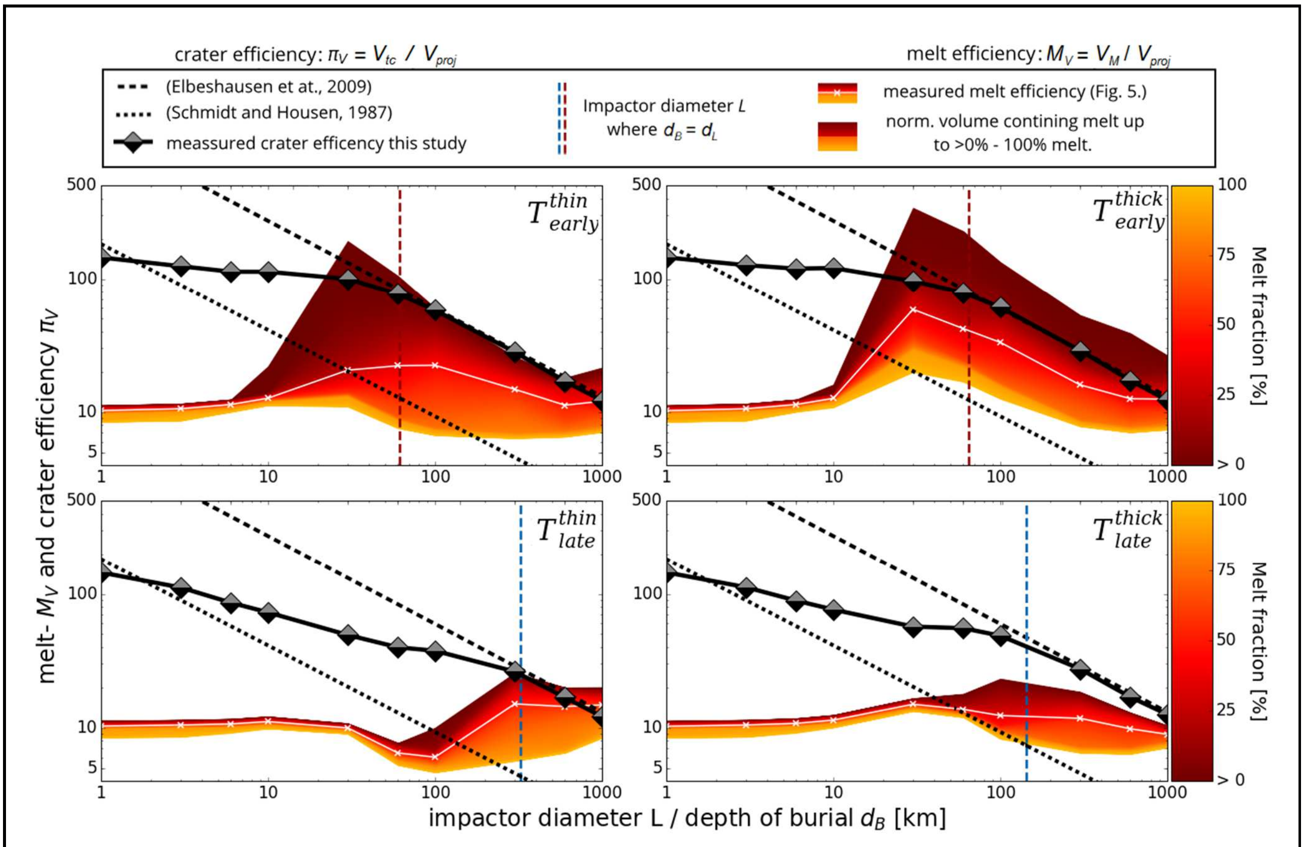

Figure 9.: Melt efficiency (M_V) compared to cratering efficiency (□$_V$) as a function of impactor diameter L for all thermal profiles (a-d) at 15 km/s. Power-laws for crater efficiency according to Elbeshausen et al. (2009) (dashed line) and Schmidt an Housen (1987) (dotted) line are compared with crater efficiency determined in models of this study (diamonds). The white line indicates the total volume of molten material normalized by the impactor volume (e.g., Fig. 5.). The colored areas indicate the volume of the region where partial melting occurs. The envelope of different colors corresponds to the volume of material where the partial melt content is at least >0% (dark red) up to 100% (yellow). The vertical dashed lines indicate where the equivalent depth of burst is equal to the depth of the lithosphere $d_B = d_L$.

Figure 9 shows cratering efficiency π_V and melt efficiency M_V as a function of impactor size. For comparison, we also show the power-laws for crater efficiency π_V according to Elbeshausen et al. (2009, dashed line) and Schmidt an Housen (1987, dotted line). Figure 9 shows that the measured transient crater volumes (black diamonds) are in good agreement with the scaling law after Schmidt and Housen (1987) for small impactors and approach the scaling law after Elbeshausen et al. (2009) for impactor sizes, where the equivalent depth of burst d_B exceeds the depth of the lithosphere d_L *(L = 30 - 300 km)*. For the early Mars T_{early}(a,b) and impactors larger than L = 10 km the melt efficiency M_V (white line) exceeds the scaled crater efficiency □$_V$ according to Schmidt and Housen (1987, dotted line). Broadly speaking, in this scenario the impact-induced melt volume exceeds the volume of the transient cavity according to the scaling law. For a late Mars, this happens for impact diameters larger than L = 100 km and L = 30 km for T_{late}^{thin} (Fig. 9c) and T_{late}^{thick} (Fig. 9d), respectively. Contrarily, the curve of the melt efficiency (white line) approaches but does not intersect the crater efficiency curve according to our simulations and the scaling law after Elbeshausen et al. (2009) except for very large collisions L = 1000 km for T_{late}^{thin} (Fig. 9c). However, melt efficiency may underestimate the final melt volume as the long-term rise of partially molten material experiences further decompression resulting in an increase of melt. To better estimate the melt production, we illustrate the volume of the region that contains partial or fully molten material. The envelope of different colors corresponds to the volume of material where the partial melt content is at least >1% (dark red) up to 100% (yellow). The volume of the entire melt region (>1% partial melting, upper boundary of the colored area) exceeds or is similar to the transient crater volume for impactor diameters larger than *L = 10 km* on early Mars (Fig. 9a,b). On late Mars, the volume of the melt region exceeds the transient crater volume only in T_{late}^{thin} (Fig. 9c) for impactor diameters larger than *L = 300 km.*

On the one hand, we consider the comparison with transient crater sizes as an upper estimate. Usually, the volume of the final crater tends to be smaller than the transient crater, especially for large craters. On the other hand, we do not account for the amount of ejected melt and we also do not distinguish between superheated melt and vapor. Overall, we interpret our results as such that complete filling of the crater structure by melt may occur at impactors larger or equal than 30 km on early Mars (T_{early}^{thick}). In some extreme cases, craters and the surroundings may be flooded by impact melt resulting in the formation of igneous provinces rather than typical basin structures. We note that our estimates suffer from the limited resolution of the overflowing melt layer (e.g. Fig 8). The comparison of melt volume with the transient crater, instead of the final crater (e.g. Fig 9) may be considered only as a preliminary approximation. In addition, for a more accurate assessment, the post impact thermodynamic evolution of melt needs to be considered, which is beyond the scope of this study.

4 Discussion:

With this study, we quantify the effect of the early thermal state of Mars on impact-induced melt production. For the first time we consider in a systematic study the contribution of decompression melting to the total generated melt volume by impact. Our results show that classical scaling laws do not provide reasonable estimates for the total melt volume on an early and thus hot Mars (4.5-3.5 Ga) for impactors larger than about 10 km in diameter. This is mainly due to the fact that geothermal gradients significantly reduce melt pressures, while decompression melting can significantly contribute to final melt production. Both aspects are usually neglected in scaling laws but should be taken into account when large impacts penetrate into warm mantle material. We find that the maximum in melt efficiency occurs when the equivalent depth of burst d_B (the depth where most of the impactors energy is deposited) exceeds or is similar to the lithosphere thickness. Broadly speaking, material at this depth requires the lowest energy input to experience melting mainly due to the shock but with increasing depth also as a consequence of lithostatic uplift. For impacts on planetary scale (L >~400 km) our results agree with previous work that accounts for the hot initial conditions and pressure dependent melting (Marinova et al. 2011).

The presented data only applies to vertical collisions. While other parameters like the cratering efficiency π_V are often approximated by using the vertical component of the impact velocity $U_\perp$ to bypass issues with the impact obliquity, this approach is not applicable for estimating the efficiency M_V (or melt volume). Pierazzo and Melosh (2000) show that the impact melt decreases by 20% for impact angles between 90° and 45° (where 90° is head-on) considering an infinite half-space as a target. For large impacts on planetary scale this relationship may change since parts of the projectile may miss the target and thus can not transfer their kinetic energy into thermal energy of the planet. For Mars, this issue was addressed by Marinova et al. (2011) where the authors found that melt volumes are reduced for impact angles between 90° to 45° by 13% and 33% for impactor diameters L = 280 and 640 km, respectively (for 15 km/s, see Fig. 12; Marinova et al., 2011). For impactors larger than L = 1000 km melt efficiency is reduced by at least 43%. Accordingly, our results may overestimate melt production by ~20% assuming the most likely impact angle of 45° considering intermediate impactor diameters (10 km < L < 400 km). In addition, the maximum of the melt efficiency M_V may be also shifted towards slightly larger impactors for oblique impacts and the effectiveness of decompression melting may be decreased. This is because the equivalent depth of burst (d_B) decreases with impact angle. Thus, larger impactors are needed to reach the depth of the lithosphere where shock melting is most efficient.

In previous studies, the formation of the Martian hemispheric dichotomy was proposed to be the result of a giant impact (e.g. Wilhelms and Squyres 1984, Nimmo et al. 2008, Marinova et al. 2008, 2011). To model the Martian lowlands, Nimmo et al. (2008) use a similar numerical approach to this study (α_{imp} = 90°, U = 14 km/s, L = 640 km) and find a melt efficiency of M_V = 4.37, which is comparable to our reference model. However, we consider the estimate of our reference model to be inaccurate as the initial temperature of the target is not taken into consideration. Our models with more realistic thermal profiles (U = 15 km/s, L = 600 km, cf. Fig 5 and 6) produce 2 - 3 times more melt relative to the scenario discussed by Nimmo et al. (2008). Depending on the geotherm, this corresponds to melt volumes of 21 - 51% of the transient crater volume, however in most of the scenarios the volume that contains melt exceeds the transient crater diameter (c.f. Fig. 9 and 6, $L = 600$). This suggests that in most of the scenarios the Borealis basin would be flooded with melt in particular if we assume that partial melt becomes buoyant (see discussion in section 3.6). The deviations to Nimmo et al. (2008) can be explained by a rather cold isothermal profile compared to the presented profiles here. Another reason for the deviations in melt volume may be related to the Tillotson equations of state that has been used by Nimmo et al. (2008) which we consider to be less accurate than the ANEOS employed in this study. A more detailed assessment of the Borealis impact is beyond the scope of our study; our maximum impact size is 1000 km and we do not account for the impact angle. To account for the elliptical appearance of the Northern Lowlands previous studies investigated oblique impact scenarios and a wider range of impactor parameters (e.g. Marinova et al. 2008, 2011). However, also scenarios suggesting mantle convection or overturn (e.g. Zhong, S. & Zuber 2001, Elkins-Tanton et al. 2005) or combination of the latter and a giant impact event (e.g. Gobalek et al. 2011) appear to be possible.

In our study we do not distinguish between impact-induced melting and vaporization, meaning that the stated melt volumes include the volume of vapor if any vapor is generated. Furthermore, all stated melt volumes are calculated by summing up by the initial pre-impact volume of the post-impact molten material. For impacts on Earth with an average impact velocity of about 20 km/s it is generally assumed that approximately the impactor and an equivalent volume of the target are vaporized (Gault et al. 1972). In terms of melt efficiency this would lower our results by a factor of two, which roughly corresponds to 2.5 - 10% vapor production depending on the melt efficiency M_V for 20 km/s impacts on Mars (c.f. Fig. 7). A similar observation can be found in Svetsov and Shuvalov (2016) where roughly 10% of the molten material is vaporized. For lower impact velocities the volume of vapor significantly decreases and is generally negligible for the given range of impact velocities used here (e.g. O'Keefe and Ahrens 1977, Svetsov and Shuvalov 2016).

Furthermore, our models do not consider the distribution of melt that is ejected upon crater excavation and thus ejected melt is not excluded from the computed melt volume. Cintala and Grieve (1998) shows by analytical considerations for the Moon that the amount of melt that remains inside the crater depends on the size of an impact event. They estimate that for an impact velocity of 15 km/s in case of small impacts (1 km transient crater diameter) most of the melt is ejected and only 30% remain inside the crater. In turn, in case of a large basin (400 km transient crater diameter) the vast majority of melt is not ejected and forms a large melt pool inside the crater. Similar figures are used by Liu et al. (2019) for Imbrium-size basins. They also estimate that >85% of the ejected melt is deposited within 5 transient crater radii, where it may get incorporated into the melt pool during crater modification. Only a very small amount of melt is ejected at velocities larger than the escape velocity. Overall, we estimate the amount of melt in the distal ejecta deposits and the escape melt volume to be small relative to the melt that remains inside the crater for the size range of impactors that has been chosen in this study.

As stated above heating and melting in the impact process is assumed to be dominated by shock compression. However, this assumption has recently been challenged by Kurosawa & Genda (2018). They show that for low-velocity impacts the contribution from plastic work is significant (see also Emsenhuber et al., 2018). Melosh & Ivanov (2018) emphasize the importance of this heat source for impact velocities below 15 km/s. Quintana et al. (2015) suggest a somewhat lower velocity threshold of 10 km/s. As we do not account for heating due to plastic work our results tend to underestimate the melt volume. However, for 20 km/s impact the heat contribution from plastic work is negligible (Kurosawa and Genda, 2018; Melosh and Ivanov, 2018). For lower velocity impacts at 15 km/s and 10 km/s we estimate an error of less than 10% and about ~25%, respectively, using the data from Kurosawa & Genda (2018), although their models are not directly comparable to the impact parameters used in this study. Kurosawa and Genda (2018) use a higher constant critical shock pressure / entropy for melting and thus a relatively high constant and pressure-independent melt temperature for comparable impact velocities. Note, despite this small inaccuracy our approach comes with other advantages (as discussed in the method section, such as less numerical diffusion and the consideration of decompression melting) that we consider to be more important and crucial for this work.

5 Conclusion:

In this work we have explored the effect of different thermal profiles on impact-induced melt production by large scale collisions throughout the early martian evolution. Our models indicate that scaling laws may result in poor melt predictions depending on the thermal profile and the impactor parameters. Thus, we conclude that the use of simple scaling laws that do not explicitly account for variations in the thermal profile should be avoided in case of an early Mars and a critical impactor diameter larger than 10 km. This conclusion may also apply to other terrestrial planets with hot interior structures.

Furthermore, our results indicate that large collisions (L >= 30 km) early in Mars' history (few 100 Myr after formation) resulted in craters that may have been completely filled with melt and in extreme cases may have been completely obliterated by their own melt. This may explain the lack of visible basin structures larger than 150 km if compared to extrapolations based on the lunar crater record, as some of those events would have resulted in the formation of an igneous province. This could help to place constraints on the cooling history of Mars, as it would require a relatively hot interior during the early stage of planetary evolution (4.4 - 4.1 Ga; Bottke and Andrews-Hanna, 2017). To address this issue in more detail further investigations are required. However, our simulations robustly show that the effect of the thermal conditions and melt production onto crater morphology can be significant if the target temperature is sufficiently close to the solidus in the equivalent depth of burst. Finally, the production of large volumes of impact melt on early Mars may have affected its atmosphere and climate via outgassing, a process that we will address in the future.

6. Acknowledgments

We thank two anonymous reviewers for their thoughtful comments that helped improve this manuscript. A.-C. P. gratefully acknowledges the financial support and endorsement from the DLR Management Board Young Research Group Leader Program and the Executive Board Member for Space Research and Technology. S. M. acknowledges the NASA Habitable Worlds Grant NNX16AR87G S002. L.M. and K.W. were funded by the German Research Foundation (DFG, SFB TRR-170-1 TP C2 and C4). This is TRR-170 contribution 96. We are grateful to Boris Ivanov, Gareth Collins and Jay Melosh for their support in developing iSALE.

Appendix A:

Table A1:

Material properties for strength model (Collins 2004) and energy for melting at normal conditions (P= 1 atm., T = 297 °K):

Parameter description:	Dunite ANEOS (Benz 1989)	Basalt ANEOS (Pierazzo 2005)
Cohesion (dam/YDAM0) [Pa]	1.0000D+04	1.0000D+04
Coeff interal friction (dam/FRICDAM)	6.0000D-01	6.0000D-01
High Pre strength limit (dam/YLIMDAM) [Pa]	3.5000D+09	2.5000D+09
Cohesion (int/YINT0) [Pa]	5.0000D+07	2.0000D+07
Coeff interal friction (int/FRICINT)	1.5000D+00	1.4000D+00
High Pre strength limit (int/YLIMINT) [Pa]	3.5000D+09	2.5000D+09

Melt energy for complete melting E_M*	8.61 x 10^6 J/kg	4.73 x 10^6 J/kg

*calculated via ANEOS and the liquidus function.

References

Abramov, O., Wong, S. M., & Kring, D. A. (2012). Differential melt scaling for oblique impacts on terrestrial planets. *Icarus*, *218*(2), 906-916.

Amsden, A. A., Ruppel, H. M., & Hirt, C. W. (1980). *SALE: A simplified ALE computer program for fluid flow at all speeds* (No. LA-8095). Los Alamos Scientific Lab., NM (USA).

Artemieva, N., & Lunine, J. I. (2005). Impact cratering on Titan II. Global melt, escaping ejecta, and aqueous alteration of surface organics. *Icarus*, *175*(2), 522-533.

Barr, A. C., & Citron, R. I. (2011). Scaling of melt production in hypervelocity impacts from high-resolution numerical simulations. *Icarus*, *211*(1), 913-916.

Benz, W., Cameron, A. G. W., & Melosh, H. J. (1989). The origin of the Moon and the single-impact hypothesis III. *Icarus*, *81*(1), 113-131.

Bierhaus, M., Wünnemann, K., & Ivanov, B. A. (2013). Affect of core rheology on shock wave propagation in planetary scale impacts. *LPICo*, *1737*, 3022.

Bjorkman, M. D., & Holsapple, K. A. (1987). Velocity scaling impact melt volume. *International Journal of Impact Engineering*, *5*(1-4), 155-163.

Bottke, W. F., & Andrews-Hanna, J. C. (2017). A post-accretionary lull in large impacts on early Mars. *Nature Geoscience*, *10*(5), 344-348.

Cintala, M. J., & Grieve, R. A. (1998). Scaling impact melting and crater dimensions: Implications for the lunar cratering record. *Meteoritics & Planetary Science*, *33*(4), 889-912.

Collins, G. S., Melosh, H. J., & Ivanov, B. A. (2004). Modeling damage and deformation in impact simulations. *Meteoritics & Planetary Science*, *39*(2), 217-231.

Collins, G. S., Wünnemann, K., Artemieva, N., & Pierazzo, E. (2013). Numerical modelling of impact processes. Impact cratering: Processes and products, 254-270.

Croft, S. K. (1982). A first-order estimate of shock heating and vaporization in oceanic impacts. *Geological Implications of Impacts of Large Asteroids and Comets on Earth*, *190*, 143-152.

Dauphas, N., & Pourmand, A. (2011). Hf–W–Th evidence for rapid growth of Mars and its status as a planetary embryo. *Nature*, *473*(7348), 489-492.

Elbeshausen, D., Wünnemann, K., & Collins, G. S. (2009). Scaling of oblique impacts in frictional targets: Implications for crater size and formation mechanisms. *Icarus*, *204*(2), 716-731.

Elkins□Tanton, L. T., Hess, P. C., & Parmentier, E. M. (2005). Possible formation of ancient crust on Mars through magma ocean processes. *J. Geophys. Res., 110, E12S01, doi:10.1029/2005JE002480.*

Emsenhuber, A., Jutzi, M., & Benz, W. (2018). SPH calculations of Mars-scale collisions: the role of the equation of state, material rheologies, and numerical effects. *Icarus*, *301*, 247-257.

Gault, D. E., Hörz, F., & Hartung, J. B. (1972). Effects of microcratering on the lunar surface. In *Lunar and Planetary Science Conference Proceedings* (Vol. 3, p. 2713).

Golabek, G. J., Keller, T., Gerya, T. V., Zhu, G., Tackley, P. J., & Connolly, J. A. (2011). Origin of the Martian dichotomy and Tharsis from a giant impact causing massive magmatism. *Icarus*, *215*(1), 346-357.

Grieve, R. A. F., & Cintala, M. J. (1992). An analysis of differential impact melt□crater scaling and implications for the terrestrial impact record. *Meteoritics*, *27*(5), 526-538.

Grieve, R. A. F., & Cintala, M. J. (1997). Planetary differences in impact melting. *Advances in Space Research*, *20*(8), 1551-1560.

Grieve, R. A. F., Cintala, M. J., & Therriault, A. M. (2006). Large-scale impacts and the evolution of the Earth's crust: The early years. *SPECIAL PAPERS-GEOLOGICAL SOCIETY OF AMERICA*, *405*, 23.

Hartmann, W. K., Malin, M., McEwen, A., Carr, M., Soderblom, L., Thomas, P., ... & Veverka, J. (1999). Evidence for recent volcanism on Mars from crater counts. *Nature*, *397*(6720), 586-589.

Holsapple, K. A. (1993). The scaling of impact processes in planetary sciences. *Annual review of earth and planetary sciences*, *21*(1), 333-373.

Ivanov, B. A., & Melosh, H. J. (2003). Impacts do not initiate volcanic eruptions: Eruptions close to the crater. *Geology*, *31*(10), 869-872.

Kleine, T., & Walker, R. J. (2017). Tungsten isotopes in planets. *Annual review of earth and planetary sciences*, *45*, 389-417.

Kurosawa, K., & Genda, H. (2018). Effects of friction and plastic deformation in shock-comminuted damaged rocks on impact heating.Geophysical Research Letters,45, 620–626.

Liu, T., Michael, G., Engelmann, J., Wünnemann, K., & Oberst, J. (2019). Regolith mixing by impacts: Lateral diffusion of basin melt. *Icarus*, *321*, 691-704.

Marchi, S., Walker, R. J., & Canup, R. M. (2020). A compositionally heterogeneous martian mantle due to late accretion. *Science Advances*, *6*(7), eaay2338.

Marinova, M. M., Aharonson, O., & Asphaug, E. (2008). Mega-impact formation of the Mars hemispheric dichotomy. *Nature*, *453*(7199), 1216-1219.

Marinova, M. M., Aharonson, O., & Asphaug, E. (2011). Geophysical consequences of planetary-scale impacts into a Mars-like planet. *Icarus*, *211*(2), 960-985.

Melosh, H. J. (1979). Acoustic fluidization: A new geologic process?. *Journal of Geophysical Research: Solid Earth*, *84*(B13), 7513-7520.

Melosh, H. J. (1989). Impact cratering: A geologic process. *Research supported by NASA. New York, Oxford University Press (Oxford Monographs on Geology and Geophysics, No. 11), 1989, 253 p.*, *11*.

Melosh, H. J., & Ivanov, B. A. (1999). Impact crater collapse. *Annual Review of Earth and Planetary Sciences*, *27*(1), 385-415.

Melosh, H. J. (2007). A hydrocode equation of state for SiO2. *Meteoritics & Planetary Science*, *42*(12), 2079-2098.

Melosh, H. J., & Ivanov, B. A. (2018). Slow impacts on strong targets bring on the heat. *Geophysical Research Letters*, *45*(6), 2597-2599.

Miljković, K., Wieczorek, M. A., Collins, G. S., Laneuville, M., Neumann, G. A., Melosh, H. J., ... & Zuber, M. T. (2013). Asymmetric distribution of lunar impact basins caused by variations in target properties. *Science*, *342*(6159), 724-726.

Miljković, K., Wieczorek, M. A., Collins, G. S., Solomon, S. C., Smith, D. E., & Zuber, M. T. (2015). Excavation of the lunar mantle by basin-forming impact events on the Moon. *Earth and Planetary Science Letters*, *409*, 243-251.

Miljković, K., Collins, G. S., Wieczorek, M. A., Johnson, B. C., Soderblom, J. M., Neumann, G. A., & Zuber, M. T. (2016). Subsurface morphology and scaling of lunar impact basins. *Journal of Geophysical Research: Planets*, *121*(9), 1695-1712.

Morbidelli, A., Nesvorny, D., Laurenz, V., Marchi, S., Rubie, D. C., Elkins-Tanton, L., Wieczorek, M. & Jacobson, S. (2018). The timeline of the lunar bombardment: Revisited. *Icarus*, *305*, 262-276.

Nimmo, F., Hart, S. D., Korycansky, D. G., & Agnor, C. B. (2008). Implications of an impact origin for the martian hemispheric dichotomy. *Nature*, *453*(7199), 1220-1223.

Ohnaka, M. (1995). A shear failure strength law of rock in the brittle-plastic transition regime: Geophysical Research Letters, v. 22, p. 25–28, doi: 10.1029/94GL02791.

O'Neill, C., Marchi, S., Zhang, S., & Bottke, W. (2017). Impact-driven subduction on the Hadean Earth. *Nature Geoscience*, *10*(10), 793-797.

O'Keefe, J. D., & Ahrens, T. J. (1977). Impact-induced energy partitioning, melting, and vaporization on terrestrial planets. In *Lunar and Planetary Science Conference Proceedings* (Vol. 8, pp. 3357-3374).

Padovan, S., Tosi, N., Plesa, A. C., & Ruedas, T. (2017). Impact-induced changes in source depth and volume of magmatism on Mercury and their observational signatures. *Nature communications*, *8*(1), 1-10.

Pierazzo, E., Vickery, A. M., & Melosh, H. J. (1997). A reevaluation of impact melt production. *Icarus*, *127*(2), 408-423.

Pierazzo, E., Artemieva, N. A., & Ivanov, B. A. (2005). Starting conditions for hydrothermal systems underneath Martian craters: Hydrocode modeling. *Large meteorite impacts III*, *443*.

Pierazzo, E., & Melosh, H. J. (2000). Melt production in oblique impacts. *Icarus*, *145*(1), 252-261.

Plesa, A. C., Grott, M., Tosi, N., Breuer, D., Spohn, T., & Wieczorek, M. A. (2016). How large are present□day heat flux variations across the surface of Mars?. *Journal of Geophysical Research: Planets*, *121*(12), 2386-2403.

Potter, R. W. K., Kring, D. A., Collins, G. S., Kiefer, W. S., & McGovern, P. J. (2012). Estimating transient crater size using the crustal annular bulge: Insights from numerical modeling of lunar basin□scale impacts. *Geophysical research letters*, *39*(18).

Potter, R. W., Kring, D. A., Collins, G. S., Kiefer, W. S., & McGovern, P. J. (2013). Numerical modeling of the formation and structure of the Orientale impact basin. *Journal of Geophysical Research: Planets*, *118*(5), 963-979.

Prieur, N. C., Rolf, T., Luther, R., Wünnemann, K., Xiao, Z., & Werner, S. C. (2017). The effect of target properties on transient crater scaling for simple craters. *Journal of Geophysical Research: Planets*, *122*(8), 1704-1726.

Quintana, S. N., Crawford, D. A., & Schultz, P. H. (2015). Analysis of impact melt and vapor production in CTH for planetary applications. *Procedia Engineering*, *103*, 499-506.

Raymond, S. N., Schlichting, H. E., Hersant, F., & Selsis, F. (2013). Dynamical and collisional constraints on a stochastic late veneer on the terrestrial planets. *Icarus*, *226*(1), 671-681.

Robbins, S. J., Di Achille, G., & Hynek, B. M. (2011). The volcanic history of Mars: High-resolution crater-based studies of the calderas of 20 volcanoes. *Icarus*, *211*(2), 1179-1203.

Roberts, J. H., & Arkani‐Hamed, J. (2014). Impact heating and coupled core cooling and mantle dynamics on Mars. *Journal of Geophysical Research: Planets*, *119*(4), 729-744.

Ruedas, T., & Breuer, D. (2017). On the relative importance of thermal and chemical buoyancy in regular and impact‐induced melting in a Mars‐like planet. *Journal of Geophysical Research: Planets*, *122*(7), 1554-1579.

Schmidt, R. M., & Housen, K. R. (1987). Some recent advances in the scaling of impact and explosion cratering. *International Journal of Impact Engineering*, *5*(1-4), 543-560.

Segura, T. L., McKay, C. P., & Toon, O. B. (2012). An impact-induced, stable, runaway climate on Mars. *Icarus*, *220*(1), 144-148.

Stöffler, D., Hamann, C., & Metzler, K. (2018). Shock metamorphism of planetary silicate rocks and sediments: Proposal for an updated classification system. *Meteoritics & Planetary Science*, *53*(1), 5-49.

Svetsov, V. V., & Shuvalov, V. V. (2016). Silicate impact-vapor condensate on the Moon: Theoretical estimates versus geochemical data. *Geochimica et Cosmochimica Acta*, *173*, 50-63.

Thompson, S. L., & Lauson, H. S. (1972). *Improvements in the Chart D radiation-hydrodynamic CODE III: Revised analytic equations of state* (No. SC-RR--71-0714). Sandia Labs..

Tonks, W. B., & Melosh, H. J. (1993). Magma ocean formation due to giant impacts. *Journal of Geophysical Research: Planets*, *98*(E3), 5319-5333.

Walker, R. J. (2009). Highly siderophile elements in the Earth, Moon and Mars: update and implications for planetary accretion and differentiation. *Geochemistry*, *69*(2), 101-125.

Wilhelms, D. E., & Squyres, S. W. (1984). The Martian hemispheric dichotomy may be due to a giant impact. *Nature*, *309*(5964), 138-140.

Wünnemann, K., Collins, G. S., & Melosh, H. J. (2006). A strain-based porosity model for use in hydrocode simulations of impacts and implications for transient crater growth in porous targets. *Icarus*, *180*(2), 514-527.

Wünnemann, K., Collins, G. S., & Osinski, G. R. (2008). Numerical modelling of impact melt production in porous rocks. *Earth and Planetary Science Letters*, *269*(3-4), 530-539.

Zhong, S., & Zuber, M. T. (2001). Degree-1 mantle convection and the crustal dichotomy on Mars. *Earth and Planetary Science Letters*, *189*(1-2), 75-84.

Zhu, M. H., Wünnemann, K., & Artemieva, N. (2017). Effects of Moon's thermal state on the impact basin ejecta distribution. *Geophysical Research Letters*, *44*(22), 11-292.